2-1-2013

The Performance of MLEM for Dynamic Imaging From Simulated Few-View, Multi-Pinhole SPECT

Dan Ma
Case Western Reserve University

Paul Arthur Wolf
Marquette University

Anne V. Clough
Marquette University, anne.clough@marquette.edu

Taly Gilat Schmidt
Marquette University, tal.gilat-schmidt@marquette.edu

Accepted version. *IEEE Transactions on Nuclear Science*, Vol. 60, No. 1 (February 2013): 115-123.

Published in final edited form as:
IEEE Trans Nucl Sci. 2013 February ; 60(1): . doi:10.1109/TNS.2012.2214235.

The performance of MLEM for dynamic imaging from simulated few-view, multi-pinhole SPECT

Dan Ma,
Department of Biomedical Engineering, Case Western University, Cleveland, OH 44105 and formerly with the Department of Biomedical Engineering, Marquette University, Milwaukee, WI, 53201, (dxm302@case.edu).

Paul Wolf,
Department of Biomedical Engineering, Marquette University, Milwaukee, WI 53201.

Anne V. Clough, and
Department of Mathematics, Statistics, and Computer Science, Marquette University, Milwaukee, WI 53201.

Taly Gilat Schmidt [Member IEEE]
Department of Biomedical Engineering, Marquette University, Milwaukee, WI 53201.

Abstract

Stationary small-animal SPECT systems are being developed for rapid dynamic imaging from limited angular views. This paper quantified, through simulations, the performance of Maximum Likelihood Expectation Maximization (MLEM) for reconstructing a time-activity curve (TAC) with uptake duration of a few seconds from a stationary, three-camera multi-pinhole SPECT system. The study also quantified the benefits of a heuristic method of initializing the reconstruction with a prior image reconstructed from a conventional number of views, for example from data acquired during the late-study portion of the dynamic TAC. We refer to MLEM reconstruction initialized by a prior-image initial guess (IG) as MLEM_{ig}. The effect of the prior-image initial guess on the depiction of contrast between two regions of a static phantom was quantified over a range of angular sampling schemes. A TAC was modeled from the experimentally measured uptake of ^{99m}Tc-hexamethylpropyleneamine oxime (HMPAO) in the rat lung. The resulting time series of simulated images was quantitatively analyzed with respect to the accuracy of the estimated exponential washin and washout parameters. In both static and dynamic phantom studies, the prior-image initial guess improved the spatial depiction of the phantom, for example improved definition of the cylinder boundaries and more accurate quantification of relative contrast between cylinders. For example in the dynamic study, there was ~50% error in relative contrast for MLEM reconstructions compared to ~25-30% error for MLEM_{ig}. In the static phantom study, the benefits of the initial guess decreased as the number of views increased. The prior-image initial guess introduced an additive offset in the reconstructed dynamic images, likely due to biases introduced by the prior image. MLEM initialized with a uniform initial guess yielded images that faithfully reproduced the time dependence of the simulated TAC; there were no statistically significant differences in the mean exponential washin/washout parameters estimated from MLEM reconstructions compared to the true values. Washout parameters estimated from MLEM_{ig} reconstructions did not differ significantly from the true values, however the estimated washin parameter differed significantly from the true value in some cases. Overall, MLEM reconstruction from few views and a uniform initial guess accurately quantified the time dependance of the TAC while introducing errors in the spatial depiction of the object. Initializing the reconstruction with a late-study initial guess improved spatial accuracy while decreasing temporal accuracy in some cases.

I. Introduction

Single Photon Emission Computed Tomography (SPECT) provides noninvasive images of the *in vivo* distribution of radiotracer molecules. Dynamic SPECT provides additional information from a time-sequence of reconstructed images, which enables estimation of kinetic parameters describing the tracer washin, washout, and retention localized in three spatial dimensions [1]–[3]. Numerous dynamic SPECT systems have been developed and used as clinical and research tools, for example, for quantifying regional cerebral blood flow, myocardial function, and renal function [4]–[9]. These dynamic systems generally measure time-activity curves on the order of minutes, because of the time required to acquire a complete set of angular views at each time point. Therefore, numerous reconstruction approaches have been developed to extract dynamic information from slowly rotating systems [3].

The first-pass uptake of some tracers occurs within seconds to minutes of injection, so that capturing the dynamics of the tracer uptake requires a system with high temporal resolution and sensitivity. Stationary multi-camera SPECT systems for small-animal imaging have been developed to enable rapid dynamic imaging by acquiring multiple projections without gantry rotation [10]–[16]. Decreasing the number of cameras reduces the cost of the system, but also decreases the azimuthal angular sampling and sensitivity of stationary systems, potentially requiring new reconstruction algorithms [17].

The feasibility of reconstructing MR and CT images from angularly undersampled data was recently studied, and several reconstruction approaches developed [18]–[21]. Several of these reconstruction algorithms rely on prior information from images that have sufficient angular sampling but limited temporal resolution. Previous work investigated reconstruction approaches for an undersampled stationary three-camera SPECT system, but did not consider the dynamic imaging task [22], [23].

The objective of this study was to quantify the performance of Maximum Likelihood Expectation Maximization (MLEM) for reconstructing a time-activity curve (TAC) with uptake duration of a few seconds from a simulated, stationary, three-camera multi-pinhole SPECT system. We also quantified the performance of a heuristic method that initializes the reconstruction with a prior image reconstructed from a conventional number of views, for example, by acquiring data during the late-study portion of the dynamic TAC where steady-state is often achieved. The effect of the prior-image initial guess on the depiction of contrast between two regions of a static phantom was quantified over a range of angular sampling schemes. A TAC was modeled from the experimentally measured uptake of ^{99m}Tc-hexamethylpropyleneamine oxime (HMPAO) in the rat lung. The resulting time series of simulated images were quantitatively analyzed with respect to the accuracy of the estimated exponential washin/washout parameters.

II. Methods and Materials

A. Few-View SPECT

The measurement process in SPECT imaging can be modeled as a linear system of equations:

$$\mathrm{g}=\mathrm{Hf} \quad (1)$$

where the vector **f** represents the discretized object, **g** represents the projection measurements, and **H** is the system matrix with H_{ij} representing the probability that a photon emitted at location j is detected in measurement i. In the absence of noise and nonideal

effects such as scatter, a unique object **f** corresponds to measurements **g** only if the rank of **H** matches the dimension of the space containing **f**. In few-view SPECT, the number of unknown parameters in the object vector, **f** is greater than the number of measurements **g**. Thus the system of equations described in Eq. 1 is underdetermined and there is an infinite set of solutions for a particular set of projections (i.e., the true solution vector plus vectors in the null space of the system matrix).

One purpose of this study was to evaluate the performance of MLEM reconstruction for few-view SPECT. The study also proposed and investigated a heuristic method for improving reconstruction from few-view SPECT by initializing the MLEM reconstruction with a prior-image obtained with high angular sampling but low temporal resolution. As described above, in few-view SPECT, the system matrix, **H**, has a nontrival null space and an infinite set of solutions, $\hat{\mathbf{f}}$, that result in the same $\mathbf{H}\hat{\mathbf{f}}$ and thus the same likelihood of having observed the measurements **g**. Therefore, in few-view SPECT, the solution arrived at by MLEM depends on the null vectors contained in the initial image guess [24]. We hypothesize that using an initial guess with high angular sampling but low temporal resolution (e.g., acquired during the late-study portion of the TAC or interlaced from few-view acquisitions during the TAC) will improve the reconstruction by introducing information about the object that is in the null space of the system matrix and cannot be obtained from the projection measurements. On the other hand, discrepancies between the initial guess and the true object may also be in the null space of **H** and could introduce errors that are not removed during reconstruction.

This study performed two sets of simulations to investigate the performance of MLEM in few-view SPECT. One study performed the simulation and reconstruction of a static phantom for a range of angular sampling schemes, where the initial guess is a reconstruction of the identical object simulated with a conventional number of views. The second study simulated a dynamic acquisition of a realistic TAC with a three-camera, nine-pinhole system. In the dynamic study, the prior-image initial guess was an image volume reconstructed from a 60-view acquisition during the late-study portion of the TAC, which does not necessarily represent the true object at all time points, yet contains substantially more angular information. For comparison, the static and dynamic phantom data were reconstructed with MLEM initialized with a uniform initial guess.

B. Simulation

The physical specifications of the simulated SPECT system are listed in Table I. Generally, the parameter values were chosen to correspond to those of rat lung imaging experiments described in Section II-E. The number of simulated cameras varied depending on the specific study, with Figure 1a depicting the three-camera system used in our dynamic simulation study. Each camera was equipped with a nine-pinhole collimator. The pinholes were arranged in an oval pattern, as illustrated in Figure 1b, with each pinhole having a 2 mm diameter and a 1 mm channel length. All pinhole channels were perpendicular to the axis of rotation. The oval arrangement was found previously to be advantageous for increasing collimator efficiency in this three-camera system configuration [25]. The pinhole collimator plate was assumed to be 20 mm of tungsten. The scintillation crystal detector was 128×128 mm^2 NaI(Tl) measuring 10 mm in thickness. The modeled crystal was not pixelated, however, detected photons were binned into 1×1-mm pixels based on their detected position. A lead cover enclosing the back and sides of the detectors was simulated to prevent background radiation from reaching the detector.

The software phantom consisted of a cylindrical object (radius = 20 mm) embedded with three cylinders of radii 5 mm (cylinder A), 6 mm (cylinder B) and 3 mm (cylinder C), as depicted in Figure 2. Details of the phantom are listed in Table 2. The phantom cavity was

modeled as water, while cylinders A-C were modeled as air, i.e., uniform activity with zero density. This phantom represents a simplistic approximation of lung tissue, which in practice has low, but non-zero density. The activity within each cylinder varied depending on the study, as described in more detail in Sections II-D and Section II-E.

Projection images were simulated with Monte Carlo methods using GATE (Geant4 Application for Emission Tomography) [26]. The Monte Carlo simulations modeled the stochastic emission of photons from the phantom and their stochastic transport through the phantom, collimator, and camera. The simulations included Compton scatter, Rayleigh scatter, and photoelectric absorption as possible interactions for the emitted 140 keV photons (^{99m}Tc), thus scatter and attenuation were modeled as part of the simulation. GATE returns the detected data in list-mode format with the detected energy of a photon equal to the sum of the energy deposited by the detected photon and its secondary particles and the photon position calculated as the energy-weighted centroid of the interactions generated by the photon [26]. The detector was modeled with ideal energy resolution and no electronic noise. For all simulations, detected photons with energy outside the 119-161 keV range were rejected as scatter, which is a larger energy window than typically used in SPECT imaging, thus representing a high-scatter case where a photon scattered at 69 degrees would be detected.

The sensitivity of pinhole collimators depends on the angle of the ray incident on the pinhole. In order to correct for the spatially-varying pinhole sensitivity during reconstruction, sensitivity maps were estimated for each pinhole of the collimator specified in Table I by simulating a flood source on the collimator surface with all but the pinhole of interest covered with tungsten [27]. The resulting projections represent the spatially-varying sensitivity of each individual pinhole and were incorporated into the reconstruction algorithm as described below.

C. Reconstruction

All reconstructions were performed using MLEM [28]. In order to correct for the spatially-varying pinhole sensitivity inherent in the system, the forward projection through each pinhole was multiplied during each iteration by the corresponding sensitivity map prior to summing the data from all pinholes [27]. The multiplicative update was again multiplied by each sensitivity map prior to backprojecting through the corresponding pinhole for each iteration. As seen in Figure 1, the multi-pinhole projections overlap somewhat on the detector plane. In general, projection overlap, or multiplexing, can potentially improve sampling while also introducing image degradations including bias and contrast-to-noise ratio reductions [29]–[31].

MLEM reconstruction was performed with two different initial image guesses. For all simulated objects, one set of reconstructions used an initial guess of a uniform cylinder of diameter 42 mm and height 42 mm, which corresponds to the field of view seen by all pinholes. We refer to reconstructions with the uniform initial guess as MLEM, and reconstructions with a prior-image initial guess (IG) as MLEM$_{ig}$. All images were reconstructed onto a 128×128×128 grid of 1×1×1 mm^3 voxels. To select the stopping iteration, the standard deviation of the voxel values was calculated within a region of interest (ROI) in cylinder A with 3-mm radius and 10 mm height. For all reconstructions, the MLEM and MLEM$_{ig}$ stopping iterations were selected to provide similar standard deviation in cylinder A.

Absolute quantification in SPECT imaging is challenging and requires correction for effects such as collimator efficiency, attenuation, and scatter [32], [33]. In order to isolate the effects of the uniform and prior-image initial guesses on the reconstruction, we considered

metrics that depend on the relative reconstructed activity rather than the absolute activity. The latter depends on the accuracy of attenuation and scatter correction algorithms, which were not performed in this study. Since these corrections were not performed, images in this study reconstructed with both MLEM and $MLEM_{ig}$ contain errors due to attenuation and scatter. The attenuation of ^{99m}Tc has been estimated as being up to 25% for rat studies, with less than 10% of the photons scattered [34]. Decay was not modeled, as the decay during the longest simulated acquisition (200 seconds) was below 1%.

The applied pinhole spatial sensitivity correction method accounts for spatially varying sensitivity, but does not provide a global correction for overall efficiency. A global correction factor could be estimated by a point source acquisition and would then scale the MLEM and $MLEM_{ig}$ reconstructed values by the same constant. Since our metrics depend on relative activity, a global efficiency scaling factor was not applied.

D. Static Phantom Study

This study considered the effects of a prior-image initial guess for the case when the prior image was a reconstruction of the identical object obtained from a larger number of views. Thus, this study provides an upper bound on the performance of the proposed method with a best-case initial guess. Cylinders A, B, and C were filled with 1.69 MBq, 1.03 MBq, and 0.47 MBq, respectively (826 Bq/mm^3 in cylinders A and C, 350 Bq/mm^3 in cylinder B). Simulations were repeated with the concentration in the background phantom cavity equal to 0%, 10% and 25% of the activity in cylinder A.

Five trials of a stationary, one-second acquisition with 3, 6, 9, 18, 27, 42 and 60 camera views (nine-pinholes per view) were simulated for each phantom configuration. To create a prior image, an acquisition of each phantom was simulated with 60 camera views and 10-seconds per view. The one-second simulation data were reconstructed with MLEM with a uniform initial guess and with the corresponding prior images as the initial guess.

Three-dimensional ROIs were extracted within each of the four cylinders in all reconstructed volumes. The ROIs for the phantom cavity and cylinders A, B, and C were of radius 3, 3, 4, and 1 mm, respectively, each of 10-mm height. The mean reconstructed value within each of the 3D ROIs was calculated for each reconstructed dataset. The ratio of reconstructed activity between the different cylinders was calculated and compared for all simulations as a measure of relative contrast.

E. Dynamic Phantom Study

This study quantified the performance of MLEM with a uniform and prior-image initial guess in depicting a typical TAC with uptake occurring over a duration of a few seconds. Because the prior image was obtained during the late-study portion of the TAC, the prior image does not necessarily represent the object at each time point.

An *in vivo* study of ^{99m}Tc-HMPAO uptake in the rat lung was performed at Zablocki VA Medical Center, under an IACUC approved protocol [35]. ^{99m}Tc-HMPAO (Ceretec ®) is a cerebral blood flow imaging agent whose tissue uptake is dependent on tissue redox status [36]. More recently, ^{99m}Tc-HMPAO uptake in the lung has been shown to be a sensitive marker of oxidant injury, and thus holds promise for early identification and assessment of clinical lung injury [37], [38]. A male Sprague-Dawley rat was anesthetized with pentobarbital sodium (40-50 mg/kg, I.P.) and the jugular vein was cannulated (PE-50 tubing). The anesthetized rat was placed supine on a plexiglass plate positioned directly on the face of a parallel-hole collimator attached to a modular gamma camera (Radiation Sensors, LLC). A 59 MBq injection of ^{99m}Tc-HMPAO was administered through the intravenous cannula and planar images were acquired every second for 45 seconds. Without

relocation, subsequent injection and imaging of 37 MBq ^{99m}Tc macroaggregated albumin (MAA) was performed. MAA particles range in size from 10-40 μm and lodge in the pulmonary capillaries in proportion to pulmonary flow on their first pass. Thus the resulting image provides a clear definition of the boundaries of the lung. A lung ROI was manually identified in the MAA images and used as a lung ROI in each of the HMPAO images. Subsequently, the mean number of counts per pixel within the lung ROI was determined from the HMPAO images and taken as the lung ROI time-activity curve (TAC). The rat was then killed by an I.V. overdose of pentobarbital.

The experimental TAC obtained from the lung ROI is shown in Figure 3. Activity in the lung was first observed in the projection images at five seconds and reached a near steady-state by 22 seconds. Measured activity at the 18 time points corresponding to the dynamic portion of the acquisition was time-shifted to begin at time zero and fit to a two-exponential model given by:

$$x(t) = \begin{cases} \alpha_1\left(1 - e^{-b_1 t}\right) & \mathrm{t} \le t_M \\ \alpha_1\left(1 - e^{-b_1 t_M}\right) - \alpha_2 + \alpha_2 e^{-b_2\left(t - t_M\right)} & \mathrm{t} > t_M \end{cases} \quad (2)$$

where t_M is the time corresponding to the peak of the curve, α_1 and α_2 control the amplitude of the curve, and b_1 and b_2 are exponential rate constants describing the rate of tracer washin and washout, respectively. Detailed pharmacokinetic modeling of HMPAO uptake involves a 4-compartment model [4]. Since the focus of this work is on image reconstruction rather than modeling of the uptake, we choose a heuristic model of the time-activity curve that effectively represented the measured data and provided exponential rate parameters for quantifying reconstruction algorithm accuracy. Throughout this work, all curve fitting was performed using the Levenberg-Marquardt algorithm (MATLAB, 2011).

The experimental TAC depicts mean counts in an ROI of a projection image acquired with a parallel-hole collimator. The experimental TAC was multiplied by the number of pixels in the lung image ROI, N_{ROI}, to calculate total detected counts originating from the lung and divided by the geometric efficiency of the parallel-hole collimator, $Ec_{parallel}$, to determine total activity in the lung, $a_{total}(t)$, as shown in Eq. 3.

$$a_{total}(t) = x(t) \cdot \frac{N_{ROI}}{Ec_{parallel}} \quad \mathrm{t} = 1, 2 \ldots 18 \quad (3)$$

The geometric efficiency of the parallel-hole collimator was calculated as [39]:

$$Ec_{parallel} = A \cdot \frac{g}{4\pi l^2} \quad (4)$$

where A is the cross-sectional area of a single collimator bore, l is the length of its channel and g is the fraction of the frontal area of the collimator that is not blocked by the collimator septa (i.e., g = total area of holes in collimator face / area of collimator face). For the collimator used in the experimental study, A = 2.4 mm^2, l = 25.4 mm, and g = 0.69. This conversion from measured counts in the projection to activity in the object did not account for attenuation during planar imaging. Thus, the simulated activity represents a lower dose (more challenging task) than the experimental protocol, although we expect this effect to be minor due to low attenuation in the rat.

Equal time-varying tracer concentrations were simulated in cylinders A and C using the modeled TAC curve. The total activity, $a_{total}(t)$ obtained from Eq. 3 above, was distributed

proportionally to the volume of each cylinder. The resulting activity concentration in cylinders A and C, in units of Bq/mm^3, is given by $a_1(t)$ in Eq. 5 and plotted in Figure 4.

$$a_1(t) = \begin{cases} 1790\left(1 - e^{-0.0647t}\right) & 0 \le t \le 9.56 \\ 404.66 + \left(1.43 \times 10^5\right) \cdot e^{-0.6097t} & \text{t}>9.56 \end{cases} \quad (5)$$

To simulate a case where the uptake distribution of the tracer within the phantom was heterogeneous, the activity in cylinder B was simulated with concentration $a_2(t)$ as given in Eq. 6 and plotted in Figure 4.

$$a_2(t) = \begin{cases} 500\left(1 - e^{-t}\right) & 0 \le t \le 5 \\ 96.63 + 659.49 \cdot e^{-0.1t} & \text{t}>5 \end{cases} \quad (6)$$

The activity in the background cylinder was equal to 40 Bq/mm^3 for all time points.

Projection images at a time-sequence of 26 one-second acquisitions, starting at time t=0.6 seconds, were simulated assuming the stationary three-camera system (without rotation) specified in Table I and depicted in Figure 1. To facilitate statistical analysis, each dynamic acquisition was simulated five times.

In addition to the dynamic simulations described above, an acquisition during the late-study phase (i.e. t ≥ 25.6 s) was also simulated with 60 camera views, i.e. 20 step-and-shoot, 10 second acquisitions with the three-camera gantry rotated over 120 degrees, assuming constant activity concentration equal to $a_1(25.6)$ = 404.7 Bq/mm^3 in cylinders A and C, $a_2(25.6)$ = 147.8 Bq/mm^3, as given by Eq. 5 and 6, and 40 Bq/mm^3 in the background cylinder.

Images were reconstructed by MLEM with a uniform initial guess (MLEM) and with the late-study prior image as an initial guess (MLEM$_{ig}$). Three-dimensional ROIs were extracted within each of the three cylinders and background cavity as in the static phantom study. The mean reconstructed value within each of the 3D ROIs was calculated at each of the 26 time points, resulting in an estimated time-activity curve, $y(t)$, for each cylinder. Overall, thirty TACs were estimated in this study, one for each of the three cylinders, simulated for each of the five trials, and obtained using each of the two reconstruction algorithms (MLEM and MLEM$_{ig}$).

In order for the SPECT system and reconstruction algorithm to faithfully reproduce the dynamic change in activity, the reconstructed activity must be linearly related to the true activity in the object. To determine the linearity of the reconstructed data, the reconstructed time-activity averaged within the ROI in each cylinder, $y(t)$, was plotted against the true time-activity, $a_1(t)$ or $a_2(t)$, for each time point, cylinder, trial, and reconstruction method. The data points from five trials of a particular cylinder were aggregated into one scatter plot and linear regression was used to evaluate the slope and offset parameters for each cylinder and reconstruction algorithm.

The relative contrast, defined as the ratio between activities in two ROIs, was calculated between all cylinders at all time points. The contrast at each time point was averaged over the five trials.

To quantify the fidelity of the reconstructed dynamic activity, each reconstructed TAC, $y(t)$, was fit to the two phase model of Eq. 2. Because the sampling of the dynamic TAC does not necessarily begin at zero seconds, an additional parameter representing time delay, t_D was

incorporated into Eq. 2 by substituting $(t - t_D)$ for t. Thus, the reconstructed TACs were fit to the modified Eq. 2 assuming six free parameters $(a_1, b_1, a_2, b_2, t_M, t_D)$, resulting in a fitted curve, $\hat{y}(t)$. The estimated washin/washout rate constants, $\hat{b}_1$ and $\hat{b}_2$, and the estimated peak time $\hat{t}_M$, were compared to the true parameters, b_1, b_2, and t_M for each cylinder, simulation trial, and reconstruction method.

III. Results

A. Static Phantom Study

Figure 5 displays the central axial slice reconstructed by MLEM for 3, 6, 9 and 60 camera views with background activity equal to 0%, 10%, and 25% of the activity in cylinder A. The image reconstructed from 60 views and ten seconds per view is also displayed for each phantom (labeled as prior image). Figure 6 displays the same images reconstructed with the prior image as the initial guess (MLEM_{ig}). Figure 7 plots the ratio of mean activity between the different cylinders for each level of angular sampling and background activity.

Comparing Figures 5 and 6, the prior-image initial guess improved the spatial depiction of the phantom, for example improved definition of the cylinder boundaries. As seen in Figure 7, quantification of the relative contrast between different cylinders was improved when using the prior-image initial guess. The benefits of the initial guess decreased as the number of views increased, supporting the hypothesis that the initial guess has a smaller effect on the reconstructed image as the system becomes more determined. Another trend to be noted in Figures 5-7 is that MLEM requires more views to match the accuracy of the 60-view image as the background activity level increases, while the MLEM_{ig} results generally converge with six views for all background activity levels. As the background activity increased, the error between the reconstructed contrast and the true contrast increased. However, this contrast error was also present in the prior image, including when the prior image was reconstructed from 120 views. For example, the true ratio between cylinders A and C equaled 1.0, whereas the MLEM_{ig} reconstructions depicted a ratio of 0.94, 1.07, and 1.14 for 0%, 10%, and 25% background activity, respectively. For comparison, the prior image depicted a relative ratio of 1.0, 1.14, and 1.19 for 0%, 10%, and 25% background activity, respectively. These results suggest that the residual error in relative contrast (0-20%) is caused by factors other than angular sampling, for example partial volume effects, attenuation, or scatter.

B. Dynamic Phantom Study

A reconstructed axial and coronal image of the phantom acquired during the late-study phase is displayed in Figure 8. The late-study image volume was reconstructed from 60 camera positions with ten seconds per view and was used subsequently as the initial guess in the MLEM_{ig} algorithm. Figure 9 compares images reconstructed by MLEM and MLEM_{ig} from the one-second acquisition at the 10^{th} time point. As described in Section II-C, the stopping iteration for each algorithm was selected such that both algorithms resulted in similar standard deviation around the mean of the voxel values in cylinder A. For example, the images depicted in Figure 9 display the fourth MLEM iteration (0.543 standard deviation) and the second MLEM_{ig} iteration (0.540 standard deviation).

Scatter plots displaying the mean reconstructed activity, $y(t)$, as a function of the true activity, $a_1(t)$ or $a_2(t)$, at each time point and cylinder are displayed in Figure 10 for the MLEM and MLEM_{ig} algorithms. The five symbols represent the five different trials for each phantom. The scatter data were fit to a straight line and the resulting fitted lines are also plotted in Figure 10. As seen in Figure 10, the values reconstructed by MLEM_{ig} contain additive offsets that are not present in the MLEM reconstructions. Also, the R^2 values were

higher for linear fits of data reconstructed by $MLEM_{ig}$, most notably for cylinder C. One observation that requires further investigation is that the linear fits for cylinders A and C differ in both slope and offset between MLEM and $MLEM_{ig}$, while differing only in offset for cylinder B.

Figures 11 and 12 compare the true relative contrast between cylinders to that estimated in images reconstructed by MLEM and $MLEM_{ig}$ at each time point. Overall, images reconstructed with $MLEM_{ig}$ demonstrated more accurate contrast measures compared to images reconstructed with MLEM. For example, the percent error in contrast, averaged across all time points, was 50% and 51% for *A/B* and *C/B*, and 29% and 25% for $MLEM_{ig}$ reconstructions, respectively. For comparison, in the late-study image reconstructed from 60 views, the percent error was 2% for A/B and 14% for *C/B*. These results suggest that the prior-image initial guess reduced the contrast error, but that substantial errors persist, likely due to the limited angular sampling of a three-camera acquisition.

The reconstructed TACs obtained from each cylinder and simulation, $y(t)$, were fit to the two phase exponential model of Eq. 2, yielding fitted curves $\hat{y}(t)$. Figure 13 shows typical reconstructed and fitted time-activity curves reconstructed with MLEM and $MLEM_{ig}$. In order to compare the shape of the estimated TAC to the true TAC, the true TAC is plotted after being scaled to have the mean value of the fitted curve. Table III lists the R^2 values resulting from fitting the reconstructed TACs to the two-exponential model. The R^2 values were significantly higher for $MLEM_{ig}$ than MLEM for all cylinders ($p< 0.05$).

Table IV compares the estimated washin, $\hat{b_1}$, washout, $\hat{b_2}$, and peak time, $\hat{t_M}$, parameters to the true value for each cylinder and reconstruction method. The washin/washout parameters estimated by MLEM reconstructions did not differ significantly from the true values for any cylinder. The washin parameter estimated by $MLEM_{ig}$ differed significantly from the true value for cylinders A and C, while the washin parameter estimated in cylinder B and the washout parameter estimated in all three cylinders did not significantly differ from the true value. For all three cylinders, an analysis of the correlation coefficients between the estimated parameters demonstrated a statistically significant ($p<0.05$) and strong ($R<-0.9$) negative correlation between parameters α_1 and b_1. This is most likely a consequence of the small value of b_1 relative to the standard deviation of reconstructed activity during the washin phase. If we consider the linearization of Eq. 2, we obtain

$$\begin{aligned} f(t) &= \alpha_1 \left(1 - e^{b_1 t}\right) \\ &\approx \alpha_1 \left(1 - (1 - b_1 t)\right) = \alpha_1 b_1 t \end{aligned} \quad (7)$$

where the lack of identifiability of α_1 versus b_1 becomes evident.

The estimated peak time, $\hat{t_M}$ differed significantly from the true value for cylinder A for MLEM reconstructions and for cylinders A and C for $MLEM_{ig}$ reconstructions. Furthermore, there were no statistically significant differences in the standard deviations of the parameter estimates obtained by the two algorithms (F-test, $p<0.05$).

IV. Discussion

In the dynamic study, MLEM reconstructions initialized with a uniform initial guess accurately depicted the general shape of the TAC and provided exponential rate parameter estimates that did not differ significantly from the true values. While the temporal distribution of activity was accurately depicted for each spatial location, the reconstructed spatial distribution contained errors when MLEM was initialized by a uniform initial guess, for example ~50% error in the contrast between cylinders and limited depiction of the

cylindtrical phantom boundaries. These spatial inaccuracies were reduced to ~25-30% by using MLEM_{ig}. A contrast error of 25-30% is relatively large compared to the error in the 60-view late-study image (2-14%), suggesting that an improved prior image or additional camera views are required to increase the reconstructed accuracy at each time point. The results of the static phantom study suggest that the benefits of the prior-image initial guess decrease as angular sampling increases.

Images reconstructed using the prior-image initial guess demonstrated an additive offset in the reconstructed values. This offset is likely caused by biases introduced by the initial guess that, along with the added edge information, are within the null space of the undersampled system matrix. This additive offset likely caused the reduced accuracy of the washin parameters, b_1, estimated from MLEM_{ig} reconstructions compared to images reconstructed with a uniform initial guess. Despite the additive offset and errors in the washin parameter, there were no statistically significant differences between the estimated and true exponential washout parameter, b_2 for MLEM_{ig} reconstructions.

Overall, the results demonstrate that MLEM with a uniform initial guess resulted in reduced accuracy in the spatial depiction of the phantom, and increased accuracy in the temporal depiction compared to images reconstructed with MLEM_{ig}. The late-study initial guess improved the spatial depiction when reconstructing from limited angular data, while potentially introducing temporal errors if the late-study image differs from the true object at a time point.

The proposed method of using a prior-image initial guess is heuristic, and thus its performance is object dependent. This study quantified the performance for the specific case of using a late-study image as the initial guess. The method is expected to be beneficial for objects whose spatial distribution remain constant during tracer uptake and washout. If, for example, a structure has complete tracer washout (voxel value equal to zero) prior to the late-study acquisition or if the object size changes between tracer uptake and the late-study phase, the late-study initial guess may be result in a less accurate image compared to reconstructions initialized by a uniform initial guess. Future studies are required to investigate the feasibility of obtaining more accurate prior images, for example by rotating the gantry during the dynamic acquisition and interlacing the resulting projections across multiple time points to create a prior image with high angular sampling and limited temporal information, as was proposed for the HighlY constrained backPRojection (HYPR) and I-HYPR algorithms [18], [19].

The proposed prior-image initial guess method has the advantage of being a simple adaptation to existing reconstruction algorithms. However, the success of the method appears dependent on the accuracy of the prior image and may increase error depending on the selected prior image. Future work is needed to implement advanced algorithms that incorporate the prior image information while being more robust to inaccuracies in the prior image. Such algorithms may incorporate a prior-image constraint as part of the reconstruction process, as has been proposed for CT imaging [20].

V. Conclusions

Angular undersampling introduced errors in the spatial depiction of the simulated phantom. These errors were reduced by using a prior image as the initial guess for MLEM reconstruction. In the dynamic study, a prior image acquired during the late-study portion of the TAC improved the spatial depiction of the dynamic phantom while introducing an offset into the reconstructed values leading to errors in the estimated washin parameter. MLEM initialized with a uniform initial guess demonstrated increased errors in the spatial depiction

of the phantom at each time point, but provided more accurate representation of the TAC at each spatial location. The MLEM$_{ig}$ algorithm provided accurate estimates of the washout parameter for all cases, but resulted errors in the washin parameter estimated in some cases. MLEM initialized with a uniform initial guess provided accurate estimates of the exponential washin/washout parameters at this rapid one-second scan interval acquired by three camera views.

Acknowledgments

This work was supported in part by NIH HL024349 and NIH 1R15CA143713-01A1. Computer simulations were performed on the Marquette University Pario High Performance Computing Cluster (NSF CTS-0521602). Thanks to Emil Sidky, PhD, (University of Chicago) for helpful discussions regarding this work.

REFERENCES

1. Celler A, Farncombe T, Bever C, Noll D, Maeght J, Harrop R, Lyster D. Performance of the dynamic single photon emission computed tomography (dSPECT) method for decreasing or increasing activity changes. Physics in Medicine and Biology. 2000; 45:3525–3543. [PubMed: 11131182]
2. Gullberg G. Dynamic SPECT imaging: exploring a new frontier in medical imaging. Biomedical Imaging: Nano to Macro, 2004. IEEE International Symposium on. Apr.2004 1:607–610. Vol. 1.
3. Gullberg G, Reutter B, Sitek A, Maltz J, Budinger T. Dynamic single photon emission computed tomography.basic principles and cardiac applications. Physics in medicine and biology. 2010; 55:R111–R191. [PubMed: 20858925]
4. Murase K, Tanada S, Fujita H, Sakaki S, Hamamoto K. Kinetic behavior of technetium-99m-HMPAO in the human brain and quantification of cerebral blood flow using dynamic SPECT. Journal of Nuclear Medicine. 1992; 33(1):135–143. [PubMed: 1730979]
5. Chiao P, Ficaro E, Dayanikli F, Rogers W, Schwaiger M. Compartmental analysis of technetium-99m-teboroxime kinetics employing fast dynamic SPECT at rest and stress. Journal of Nuclear Medicine. 1994; 35(8):1265–1273. [PubMed: 8046477]
6. Celler A, Bong J, Blinder S, Attariwala R, Noll D, Hook L, Farncombe T, Harrop R. Preliminary results of a clinical validation of the dSPECT method for determination of renal glomerular filtration rate (GFR). Nuclear Science Symposium Conference Record, 2001 IEEE. Nov.2001 2:1079–1082. vol.2.
7. Liu Z, Stevenson G, Barrett H, Kastis G, Bettan M, Furenlid L, Wilson D, Woolfenden J. Imaging recognition of multidrug resistance in human breast tumors using 99mTc-labeled monocationic agents and a high-resolution stationary SPECT system. Nuclear Medicine and Biology. 2004; 31(1): 53–65. [PubMed: 14741570]
8. Feng B, Pretorius P, Farncombe T, Dahlberg S, Narayanan M, Wernick M, Celler A, Leppo J, King M. Simultaneous assessment of cardiac perfusion and function using 5-dimensional imaging with Tc-99m teboroxime. 13. Journal of Nuclear Cardiology. 2006; (3):354–361.
9. Niu X, Yang Y, King M, Wernick M. Detectability of perfusion defect in five-dimensional gated-dynamic cardiac SPECT images. Medical Physics. 2010; 37:5102–5113. [PubMed: 20964230]
10. Liu Z, Kastis G, Stevenson G, Barrett H, Furenlid L, Kupinski M, Patton D, Wilson D. Quantitative analysis of acute myocardial infarct in rat hearts with ischemia-reperfusion using a high-resolution stationary SPECT system. Journal of Nuclear Medicine. 2002; 43(7):933–939. [PubMed: 12097466]
11. Peterson T, Kim H, Crawford M, Gershman B, Hunter W, Barber H, Furenlid L, Wilson D, Woolfenden J, Barrett H. Semispect: a small-animal imaging system based on eight cdznte pixel detectors. Nuclear Science Symposium Conference Record, 2002 IEEE. Nov.2002 3:1844–1847.
12. Beekman F, Vastenhouw B. Design and simulation of a high-resolution stationary SPECT system for small animals. Physics in Medicine and Biology. 2004; 49:4579–4592. [PubMed: 15552418]
13. Furenlid L, Wilson D, Chen Y, Kim H, Pietraski P, Crawford M, Barrett H. FastSPECT II: a second-generation high-resolution dynamic SPECT imager. IEEE Transactions on Nuclear Science. 2004; 51(3):631–635. [PubMed: 20877439]

14. Beekman F, van der Have F, Vastenhouw B, van der Linden A, van Rijk P, Burbach J, Smidt M. U-SPECT-I: a novel system for submillimeter-resolution tomography with radiolabeled molecules in mice. Journal of Nuclear Medicine. 2005; 46(7):1194. [PubMed: 16000289]
15. Funk T, Després P, Barber W, Shah K, Hasegawa B. A multipinhole small animal SPECT system with submillimeter spatial resolution. Medical Physics. 2006; 33:1259–1269. [PubMed: 16752560]
16. Hesterman J, Kupinski M, Furenlid L, Wilson D, Barrett H. The multi-module, multi-resolution system (M3R): A novel small-animal SPECT system. Medical Physics. 2007; 34:987–994. [PubMed: 17441245]
17. Kagadis GC, Loudos G, Katsanos K, Langer SG, Nikiforidis GC. In vivo small animal imaging: Current status and future prospects. Med. Phys. 2010; 37(12):6421–6442. [PubMed: 21302799]
18. Mistretta C, Wieben O, Velikina J, Block W, Perry J, Wu Y, Johnson K. Highly constrained backprojection for time-resolved MRI. Magnetic Resonance in Medicine. 2006; 55(1):30–40. [PubMed: 16342275]
19. O'Halloran R, Wen Z, Holmes J, Fain S. Iterative projection reconstruction of time-resolved images using highly-constrained back-projection (HYPR). Magnetic Resonance in Medicine. 2008; 59(1):132–139. [PubMed: 18058939]
20. Chen G, Tang J, Leng S. Prior image constrained compressed sensing (PICCS): a method to accurately reconstruct dynamic CT images from highly undersampled projection data sets. Medical Physics. 2008; 35:660–664. [PubMed: 18383687]
21. Sidky E, Pan X. Image reconstruction in circular cone-beam computed tomography by constrained, total-variation minimization. Physics in Medicine and Biology. 2008; 53:4777–4807. [PubMed: 18701771]
22. Hsieh H-H, Lin K-J, Hsu C-H, Hsiao I-T. Performance evaluation on reconstructions in a stationary multi-pinhole spect. Nuclear Science Symposium Conference Record (NSS/MIC), 2009 IEEE. Nov 1.2009 24:3777–3780. 2009.
23. Hsieh H, Hsiao I. Image reconstructions from limit views and angle coverage data for a stationary multi-pinhole spect system. Tsinghua Science and Technology. 2010; 15(1):44–49. [Online]. Available: http://www.sciencedirect.com/science/article/pii/S1007021410700079.
24. Barrett, HH.; Myers, KJ. Foundations of Image Science. Wiley-Interscience; 2004.
25. Ma D, Clough A, Schmidt T. Multi-pinhole dynamic SPECT imaging: simulation and system optimization. Proceedings of SPIE. 2010; 7622:76220U.
26. Jan S, Santin G, Strul D, Staelens S, Assie K, Autret D, Avner S, Barbier R, Bardies M, Bloomfield P, et al. GATE: a simulation toolkit for PET and SPECT. Physics in Medicine and Biology. 2004; 49:4543–4561. [PubMed: 15552416]
27. Vanhove C, Defrise M, Lahoutte T, Bossuyt A. Three-pinhole collimator to improve axial spatial resolution and sensitivity in pinhole spect. European Journal of Nuclear Medicine and Molecular Imaging. 2008; 35:407–415. 10.1007/s00259-007-0579-y. [Online]. Available: http://dx.doi.org/10.1007/s00259-007-0579-y. [PubMed: 18000667]
28. Shepp L, Vardi Y. Maximum likelihood reconstruction for emission tomography. IEEE Trans. Med. Imaging. 1982; 1(2):113–122. [PubMed: 18238264]
29. Vunckx K, Suetens P, Nuyts J. Effect of overlapping projections on reconstruction image quality in multipinhole SPECT. Medical Imaging, IEEE Transactions on. 2008; 27(7):972–983.
30. Mok G, Wang Y, Tsui B. Quantification of the multiplexing effects in multi-pinhole small animal spect: A simulation study. Nuclear Science, IEEE Transactions on. Oct; 2009 56(5):2636–2643.
31. Mok G, Tsui B, Beekman F. The effects of object activity distribution on multiplexing multi-pinhole SPECT. Physics in medicine and biology. 2011; 56:2635–2650. [PubMed: 21454926]
32. Ritt P, Vija H, Hornegger J, Kuwert T. Absolute quantification in spect," European Journal of Nuclear Medicine and Molecular Imaging. 2011; 38:69–77. 10.1007/s00259-011-1770-8. [Online]. Available: http://dx.doi.org/10.1007/s00259-011-1770-8.
33. Wu C, van der Have F, Vastenhouw B, Dierckx R, Paans A, Beekman F. Absolute quantitative total-body small-animal SPECT with focusing pinholes. European Journal of Nuclear Medicine and Molecular Imaging. 2010; 37:2127–2135. 10.1007/s00259-010-1519-9. [Online]. Available: http://dx.doi.org/10.1007/s00259-010-1519-9. [PubMed: 20577738]

34. Hwang A, Franc B, Gullberg G, Hasegawa B. Assessment of the sources of error affecting the quantitative accuracy of SPECT imaging in small animals. Physics in Medicine and Biology. 2008; 53:2233–2252. [PubMed: 18401059]

35. Clough A, Haworth S, Audi S, Roerig D. Differential Uptake of SPECT Agents in Rat Lungs. American Journal of Respiratory and Critical Care Medicine. 2009; 179:A1058.

36. Sharp PF, Smith FW, Gemmell HG, Lyall D, Evans NTS, Gvozdanovic D, Davidson J, Tyrell DA, Pickett RD, Neirinckx RD. Technetium-99m hm-pao stereoisomers as potential agents for imaging regional cerebral blood flow: Human volunteer studies. J. Nucl. Med. 1986; 27(2):171–177. [PubMed: 3712035]

37. Jacquier-Sarlin M, Polla B, Slosman D. Oxido-reductive state: The major determinant for cellular retention of technetium-99m-hmpao. Journal of Nuclear Medicine. 1996; 37(8):1413–1416. [Online]. Available: http://jnm.snmjournals.org/content/37/8/1413.short. [PubMed: 8708786]

38. Suga K, Uchisako H, Nishigauchi K, Shimizu K, Kume N, Yamada N, Nakanishi T. Technetium-99m-hmpao as a marker of chemical and irradiation lung injury: Experimental and clinical investigations. Journal of Nuclear Medicine. 1994; 35(9):1520–1527. [Online]. Available: http://jnm.snmjournals.org/content/35/9/1520.short. [PubMed: 8071704]

39. Bushberg, J.; Seibert, J.; Leidholdt Jr, E.; Boone, J.; Goldschmidt Jr, E. The Essential Physics of Medical Imaging. 2nd ed.. Lippincott Williams & Wilkins; Baltimore, MD: 2002. ch. 21

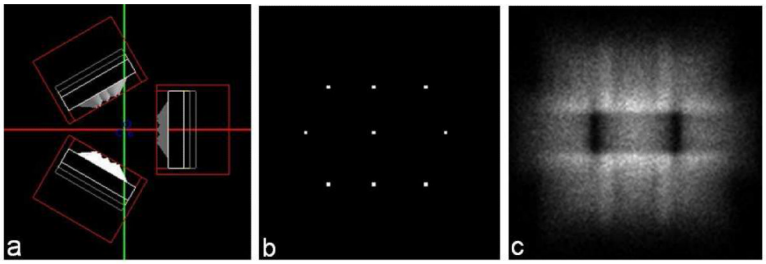

Fig. 1.

(a) Transverse view of the simulated SPECT system with three cameras (red wireframe) at 120-degree intervals. (b) The arrangement of pinholes on the collimator. All pinhole channels were perpendicular to the axis of rotation. (c) Simulated projection of phantom described in Table II.

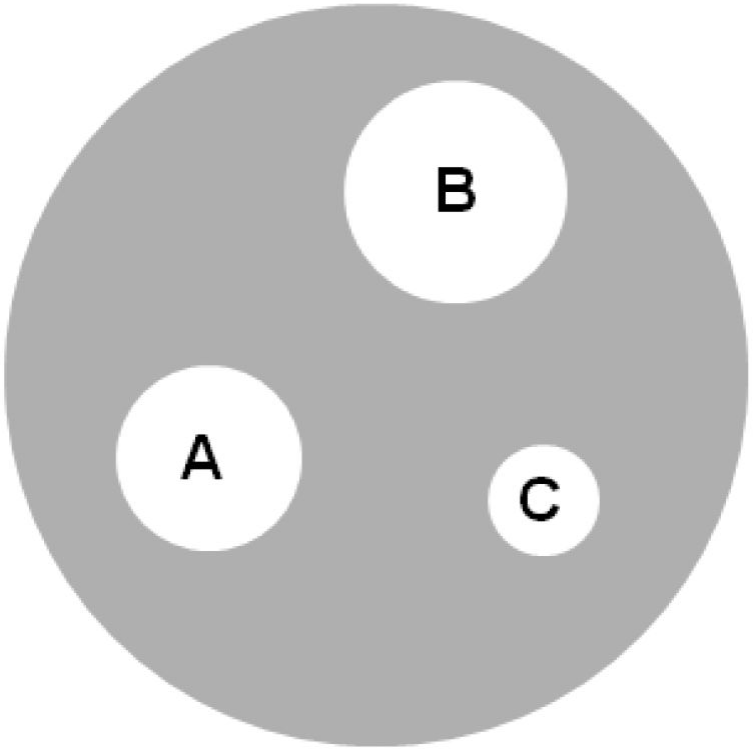

Fig. 2.
Cross-section of the simulated rat-lung phantom. The gray region was water filled with activity while the three white cylinders were air filled with activity.

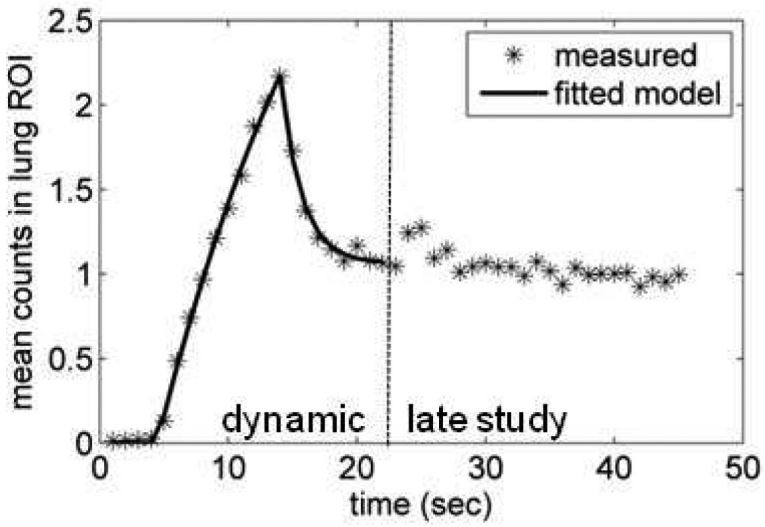

Fig. 3.

Experimental ^{99m}Tc-HMPAO time-activity curve obtained from the lung ROI, partitioned into the dynamic and late-study phases. The dynamic portion of the curve (seconds 5-22) was fit to a two-exponential model (solid line).

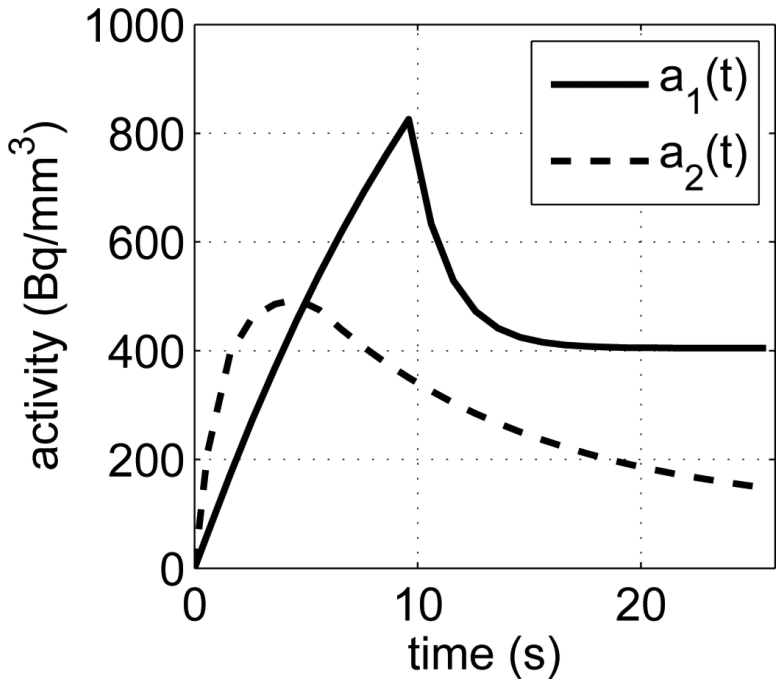

Fig. 4.

The two time activity curves simulated within the phantom cylinders. The curve $a_1(t)$ is modeled from the experimentally measured uptake of ^{99m}Tc-HMPAO in the rat lung.

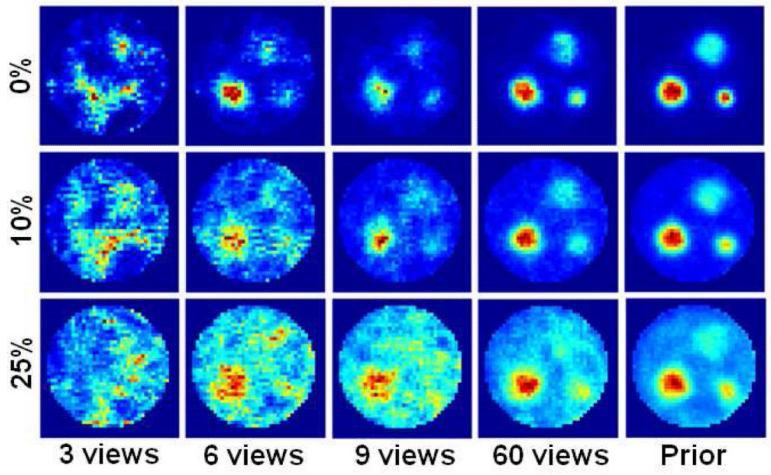

Fig. 5.

Central axial slice of the phantom reconstructed by MLEM (uniform initial guess) from a varying number of views and background activity levels acquired at one view per second. For comparison, an image reconstructed from 60 views each acquired over 10 seconds per view is also displayed and labeled as ‘prior.’ The images are scaled to display the full dynamic range in each slice.

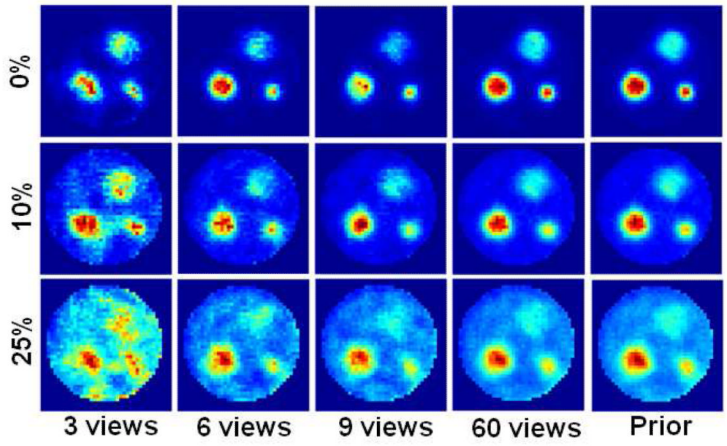

Fig. 6.

Central axial slice of the phantom reconstructed by MLEM$_{ig}$ from a varying number of views and background activity levels acquired at one view per second. The initial guess was the volume reconstructed from 60 camera views each over 10 seconds, labeled as the prior image in the figure. The images are scaled to display the full dynamic range in each slice.

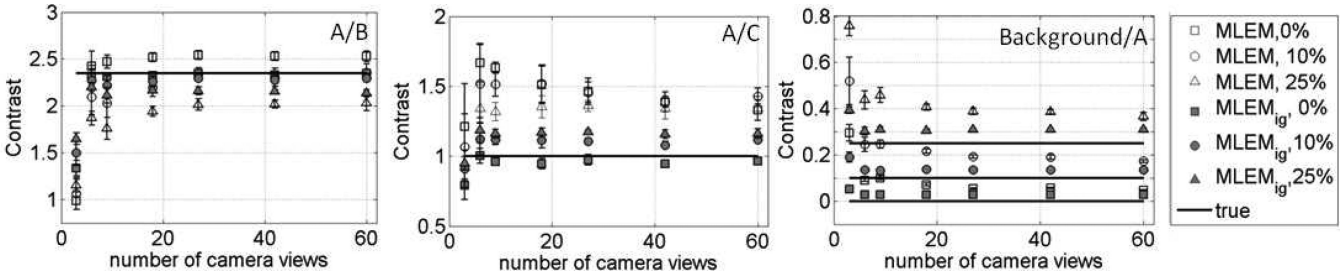

Fig. 7.

Ratio of activity between cylinders (left) A/B, (center) A/C, and (right) background/A, resulting from MLEM and MLEM$_{ig}$ reconstructions of simulations with varying angular sampling and background activity levels. The true ratio is plotted as a solid line. In the rightmost plot (Background/A), the true contrast for the three simulated cases is plotted as horizontal lines at 0%, 10%, and 25% relative contrast. The error bars represent one standard deviation.

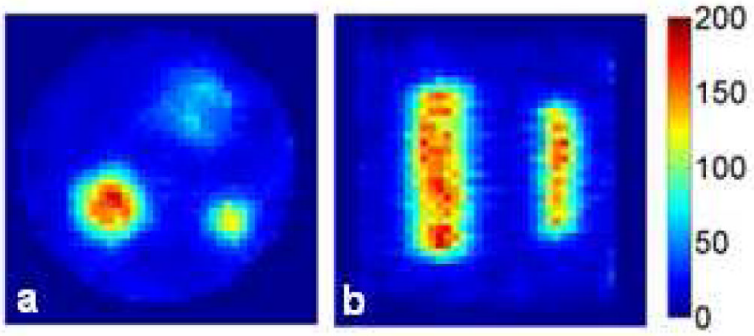

Fig. 8.

(a) Axial and (b) coronal images reconstructed by MLEM for the late-study acquisition with 60 camera views with 10 seconds per view. The axial image represents the central axial slice, while the coronal image is located at the center of cylinder C. Voxel values are in units of Bq/mm^3.

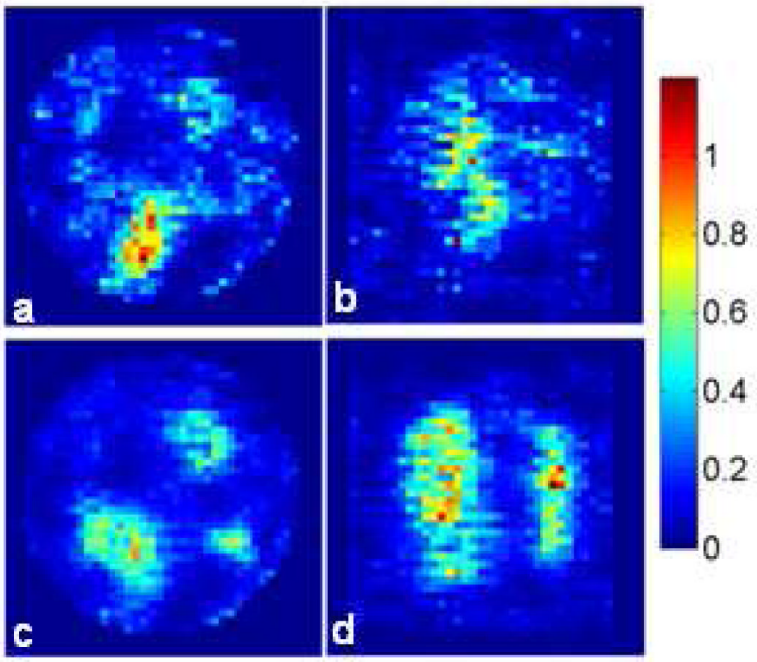

Fig. 9.

(a) Axial and (b) coronal images reconstructed by MLEM and (c) axial and (d) coronal images reconstructed by $MLEM_{ig}$ for the one-second, three camera acquisition at the 10^{th} time point. The axial image represents the central axial slice, while the coronal image is located at the center of cylinder C. Voxel values are in units of Bq/mm^3.

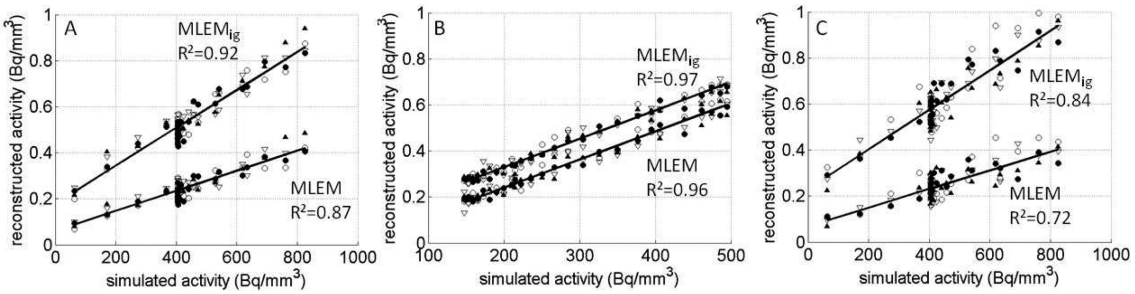

Fig. 10.

Scatter plots of the mean reconstructed activity versus simulated activity for each cylinder (A,B,C) reconstructed at each time point with MLEM and MLEM$_{ig}$. The five symbols represent the five different trials for each phantom. The estimated linear fits are also plotted.

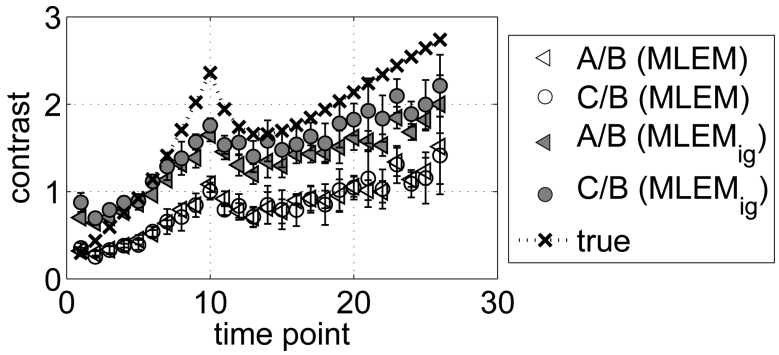

Fig. 11.

The ratio between mean reconstructed values (relative contrast) in cylinders A and B (A/B) and cylinders C and B (C/B) in images reconstructed by MLEM and MLEM$_{ig}$. The error bars represent one standard deviation. The true ratios are also plotted.

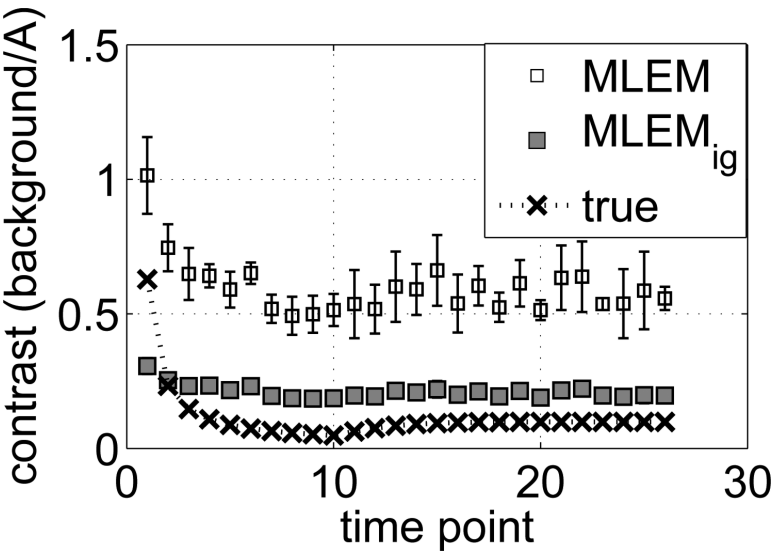

Fig. 12.

The ratio between mean reconstructed values in an ROI within the background and in cylinder A reconstructed by MLEM and MLEM$_{ig}$. The error bars represent one standard deviation.

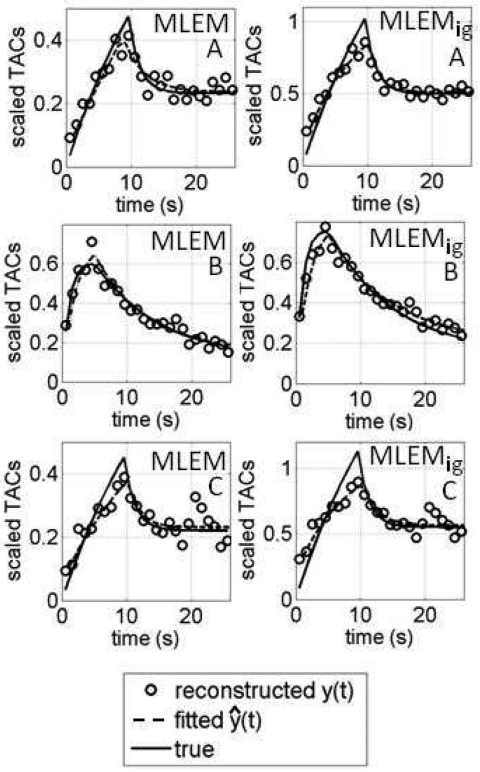

Fig. 13.

The tracer activity, $y(t)$, reconstructed by MLEM and MLEM$_{ig}$ at the 26 time points for cylinders A, B, and C. Also plotted are the resulting fits to the two-exponential model, $\hat{y}(t)$, and the true curve scaled to have the mean value of the fitted curve.

TABLE I

Specifications of the simulated SPECT system and collimator

Camera Face	128 mm × 128 mm
Number of camera pixels	128 × 128
Pinhole diameter	2 mm
Pinhole-to-object distance	53.5 mm
Pinhole-to-detector distance	45 mm
Pinhole positions	(21.3, 0) (−21.3, 0) (15, 15) (15, −15) (−15, −15) (−15, 15) (0, 15) (0, −15), (0, 0)

TABLE II

Phantom Specifications

	Center (mm)	Height (mm)	Radius (mm)
Phantom cavity	(0,0)	40	20
Cylinder A	(−7.4,−5.4)	26	5
Cylinder B	(5.4,8.8)	26	6
Cylinder C	(10.2,−7.4)	20	3

TABLE III

R^2 values resulting from fitting the reconstructed TACs to the two-exponential model, averaged across all five trials for each cylinder (mean ± standard deviation).

	A	B	C
MLEM	0.89 ± 0.04	0.97 ± 0.01	0.78 ± 0.04
MLEM $_{ig}$	0.95 ± 0.01	0.98 ± 0.01	0.89 ± 0.03

TABLE IV

Comparison of true washin, washout, and peak time parameters, (b_1, b_2, t_M) and the parameters estimated from the reconstructed data, ($\hat{b_1}$, $\hat{b_2}$, $\hat{t_M}$). (MEAN ± STANDARD DEVIATION)

		A	B	C
$\mathbf{b}_1$	**True**	0.0647	1.000	0.0647
	MLEM	0.073 ± 0.067	1.18 ± 0.58	0.056± 0.05
	MLEM $_{ig}$	0.136± 0.046	0.96 ± 0.33	0.11 ± 0.05
$\mathbf{b}_2$	**True**	0.6097	0.100	0.6097
	MLEM	1.13 ± 1.14	0.11 ± 0.02	0.52 ± 0.42
	MLEM $_{ig}$	0.89 ± 0.63	0.10 ± 0.01	0.51 ± 0.22
$\mathbf{t}_M$	**True**	9.56	5.00	9.56
	MLEM	10.8 ± 0.78	4.66 ± 0.73	10.0 ± 1.12
	MLEM $_{ig}$	11.1 ± 0.6	5.37 ± 0.44	11.0 ± 0.6